Topological Spaser

Jhih-Sheng Wu,* Vadym Apalkov,† and Mark I. Stockman‡
Center for Nano-Optics (CeNO) and Department of Physics and Astronomy, Georgia State University, Atlanta, Georgia 30303, USA

(Received 1 October 2019; published 6 January 2020)

We theoretically introduce a topological spaser, which consists of a hexagonal array of plasmonic metal nanoshells containing an achiral gain medium in their cores. Such a spaser can generate two mutually time-reversed chiral surface plasmon modes in the **K** and **K**′ valleys, which carry the opposite topological charges, ± 1, and are described by a two-dimensional E' representation of the D_{3h} point symmetry group. Due to the mode competition, this spaser exhibits a bistability: only one of these two modes generates, which is a spontaneous symmetry breaking. Such a spaser can be used for an ultrafast all-optical memory and information processing, and biomedical detection and sensing with chirality resolution.

DOI: 10.1103/PhysRevLett.124.017701

The concept of the surface plasmon amplification by stimulated emission of radiation (plasmonic nanolaser) [1–3] has recently been experiencing rapid development. Spaser is similar to laser but the population inversion is used to amplify surface plasmons (SPs) and not photons, which allows for nanoscopic spasers. Many different types of spasers have been proposed [4–7] and demonstrated [8–18]. The spasers were also applied to various problems including explosives detection [19], monitoring of the nanoenvironment [20,21], cancer therapeutics and diagnostics (theranostics) [22].

Some spasers are plasmonic crystals that include gain media [7,13,23,24]. These belong to the class of lasing spasers [7], which are nanostructured plasmonic metasurfaces consisting of a periodic lattice of individual spasers. Due to interactions in the near field, the individual spasers lock in phase to generate temporally and spatially coherent fields. However, such a fundamental question as the effects of topological properties (the Berry curvature) [25,26] of the plasmonic Bloch bands has not yet been investigated.

Recently, a ground-breaking work has been carried out to obtain a topological lasing in a plasmonic-photonic (diffractive) lattice of honeycomb symmetry [27]. The plasmonic lasing was observed at the **K** points but only in a mode of the A_1' symmetry, which is a singlet representation that does not possess a chiral topological charge.

In this Letter, we propose a topological spaser that is a deeply subwavelength two-dimensional (2D) crystal (metasurface) with a honeycomb symmetry built of two different triangular sublattices, *A* and *B*—see Fig. 1. A meta-atom of such a lattice is a plasmonic metal nanoshell containing an achiral gain medium, similar to the spaser of Ref. [3]. The *A* and *B* sublattices of such a topological spaser differ in size and shape of the constituent nanoshells (see the caption to Fig. 1), so their individual spasers have different eigenfrequencies. A natural example of a honeycomb lattice consisting of two different sublattices is provided by the transition metal dichalcogenide (TMDC) crystals [28–30].

The spasing eigenmodes are SPs that should be classified corresponding to irreducible representations of the symmetry point group of the lattice, which is D_{3h} [31]. This group has six representations, of which E' is a two-dimensional (doublet) representation with the desired properties—see the Supplemental Material [32]. It describes two degenerate modes time-reversed to each other, which carry topological charges of $Q_T = \pm 1$ defining their chirality; their local fields rotate in time and space in the opposite directions.

For the proposed topological spaser, we will show that the degenerate eigenmodes at the **K** and **K**′ points strongly

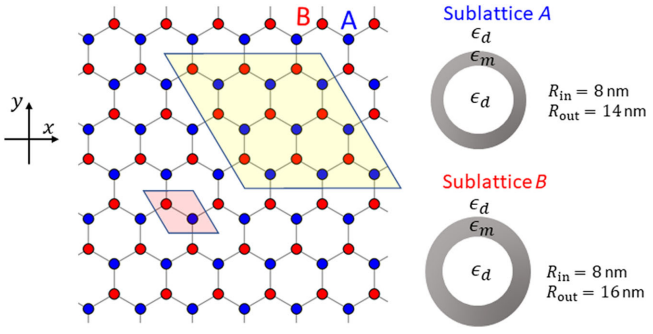

FIG. 1. Honeycomb array of metal nanoparticles built of two inequivalent sublattices: *A* and *B*. Sublattice *A* consists of plasmonic metal nanoshells with the inner radius of 8 nm and the outer radius of 14 nm while sublattice *B* consists of similar nanoshells with the inner radius of 8 nm and the outer radius of 16 nm. The gain medium is placed inside the nanoshells. The lattice bond length is set as 50 nm. The primitive unit cell of the honeycomb crystal structure is shown by the red parallelogram. The supercell, which describes the periodicity of the SPs at both the **K** and **K**′ points, see Eqs. (9)–(12), is marked by the yellow parallelogram.

compete with each other, making such a spaser bistable: either $Q_T = 1$ or $Q_T = -1$ mode can generate. These spasing modes are topological Berry plasmons [33]. However, in Ref. [33], the system's chirality was due to the induced valley polarization. In a sharp contrast, in our case the system is originally achiral and $\mathcal{T}$ reversible: no integral Berry curvature or magnetic field are present; the chirality is self-organized due to the mode competition causing a spontaneous violation of the $\mathcal{T}$ reversal and σ_v'-reflection symmetries.

The quasistatic SPs' eigenmodes [34] are electric potentials, $\varphi_{\nu\mathbf{k}}(\mathbf{r})$, characterized by lattice momentum $\mathbf{k}$ and band index ν, which can be found from the quasistatic equation [35]

$$\nabla[\Theta(\mathbf{r})\nabla\varphi_{\nu\mathbf{k}}(\mathbf{r})] = s_{\nu\mathbf{k}}\nabla^2\varphi_{\nu\mathbf{k}}(\mathbf{r}), \tag{1}$$

where $1 > s_{\nu\mathbf{k}} > 0$ are the eigenvalues, and $\Theta(\mathbf{r})$ is the characteristic function, which is 1 inside and 0 outside the metal. These satisfy an orthonormality condition: $\int \nabla\varphi_{\nu\mathbf{k}}\nabla\varphi^*_{\nu'\mathbf{k}'}d^3r = \delta_{\nu\nu'}\delta_{\mathbf{k}\mathbf{k}'}$.

We employ the tight-binding approximation where the on site states are the modes of isolated metal nanoshells, and the coupling between them is the nearest-neighbor dipole interaction. For each nanoshell, we consider two eigenmodes constituting a basis for the E' doublet representation of the D_{3h} point symmetry group, $\varphi_m^{(\alpha)} \propto Y_{1m}$, where Y_{1m} are the spherical harmonics, $m = \pm 1$, and $\alpha = A$ or B. These eigenmodes have the electric fields in the xy plane of the lattice and are coupled by the dipole interaction.

The eigenmodes $\varphi_m^{(\alpha)}$ of an isolated nanoshell of a sublattice $\alpha = A$, B satisfy the following equation [cf. Eq. (1)]

$$\nabla[\Theta^{(\alpha)}(\mathbf{r})\nabla\varphi_m^{(\alpha)}(\mathbf{r})] = s_m^{(\alpha)}\nabla^2\varphi_m^{(\alpha)}(\mathbf{r}), \tag{2}$$

where $\Theta^{(\alpha)}(\mathbf{r})$ is 1 inside the metal of nanoshell α and 0 elsewhere, and $\mathbf{r}$ is relative to the center of this nanoshell. The solution of Eq. (2) can be expressed as an expansion over the spherical harmonics, Y_{1m}, see the Supplemental Material [32].

We express the quasistatic potential for a mode with quantum numbers $\nu, \mathbf{k}$ as a sum over the lattice and $m = \pm 1$,

$$\varphi_{\nu\mathbf{k}}(\mathbf{r}) = \sum_{j\alpha m} C^{(\alpha)}_{\nu\mathbf{k}m}\sqrt{s_m^{(\alpha)}}\exp(i\mathbf{k}\mathbf{R}_j^{(\alpha)})\varphi_m^{(\alpha)}(\mathbf{r} - \mathbf{R}_j^{(\alpha)}), \tag{3}$$

where $\mathbf{R}_j^{(\alpha)}$ is the lattice vector of the nanoshell j center in sublattice α. Expansion coefficients $C^{(\alpha)}_{\nu\mathbf{k}m}$ satisfy the tight-binding equations

$$\sum_{\alpha' m'} H_{\alpha m,\alpha' m'}(\mathbf{k}) C^{(\alpha')}_{\nu\mathbf{k}m'} = s_{\nu\mathbf{k}} C^{(\alpha)}_{\nu\mathbf{k}m}. \tag{4}$$

Here the nearest-neighbor tight-binding Hamiltonian is

$$H_{\alpha m,\alpha' m'} = \begin{cases} s_m^{(\alpha)}\delta_{mm'}, & \alpha = \alpha', \\ \sqrt{s_m^{(\alpha)}}\sqrt{s_{m'}^{(\alpha')}}\sum_{j'}\exp[i\mathbf{k}(\mathbf{R}^{\alpha}_{j'} - \mathbf{R}^{\alpha}_{j})]\times & \\ \int \nabla\varphi_m^{(\alpha)*}(\mathbf{r} - \mathbf{R}_j^{(\alpha)})\nabla\varphi_m^{(\alpha')}(\mathbf{r} - \mathbf{R}_{j'}^{(\alpha')})d^3r, & \alpha \neq \alpha', \end{cases} \tag{5}$$

where j denotes a lattice site, and j' are the nearest-neighbor sites.

The solution of Eq. (4) produces four bands whose dispersions are shown in Fig. 2(a). Due to the broken inversion symmetry owing to the sublattices A and B being inequivalent, there are band gaps opened at the $\mathbf{K}$ and $\mathbf{K}'$ points.

The structure of SPs at these points is the following. At either the $\mathbf{K}$ point or the $\mathbf{K}'$ point, the SP modes are excited in the real space only on a single sublattice A—see an illustration in Fig. 2(b). The SPs at the $\mathbf{K}$ and $\mathbf{K}'$ points are mutually time reversed: the magnetic quantum numbers are $m = \pm 1$ corresponding to the topological charges $Q_T = \pm 1$, and the phase shifts between the nearest sites on the A sublattice are $\pm 2\pi/3$, respectively—see Figs. 3(a)–3(d). Below we assume that the frequency of the optical transitions in the gain medium is equal to the frequency of SPs in the valence band at the $\mathbf{K}$ and $\mathbf{K}'$ points—see Fig. 3(e).

The SPs at the $\mathbf{K}$ and $\mathbf{K}'$ points have equal frequencies, $\omega_{\nu\mathbf{K}} = \omega_{\nu\mathbf{K}'}$, as protected by the $\mathcal{T}$ symmetry. We write down the SP Hamiltonian in the second quantization as

$$H_{\mathrm{SP}} = \hbar\omega_{\nu\mathbf{K}}(\hat{a}^\dagger_{\nu\mathbf{K}}\hat{a}_{\nu\mathbf{K}} + \hat{a}^\dagger_{\nu\mathbf{K}'}\hat{a}_{\nu\mathbf{K}'}), \tag{6}$$

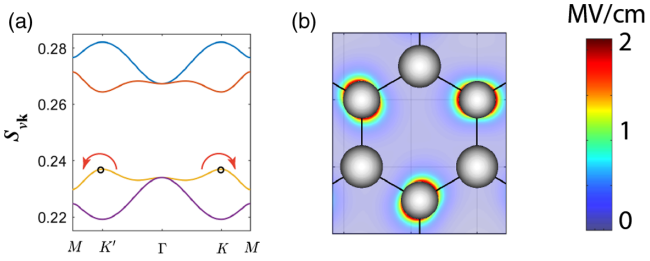

FIG. 2. (a) Band structure of honeycomb array of metal nanoshells. Due to the broken inversion symmetry, there are band gaps at the $\mathbf{K}$ and $\mathbf{K}'$ points. The spasing SP modes at the $\mathbf{K}$ and $\mathbf{K}'$ points are indicated by open circles; the arrows indicate the direction of the rotation of the local modal fields for the corresponding valleys. (b) Snapshot of profile of an SP electric field at the valence band in the $\mathbf{K}$ valley at a certain instance of time. Only the SPs at sublattice A are excited. The color bar to the right codes the modal field amplitude.

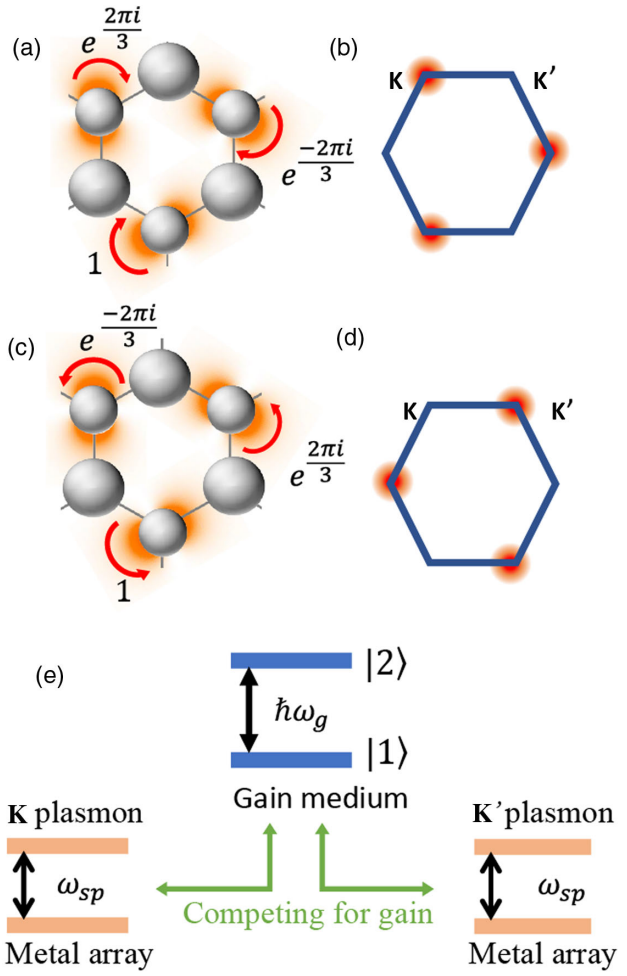

FIG. 3. (a)–(d) The valence band SPs in the $\mathbf{K}$ and $\mathbf{K}'$ valleys. For both the valleys, only the SPs at the sublattice A are excited. For the $\mathbf{K}$ valley, these are the SPs with $m = 1$, while for the $\mathbf{K}'$ valley, the SP with $m = -1$ are generated. Their phase shifts from site to site are $\pm 2\pi/3$, respectively. The SP local fields rotate in the directions shown by the red arrows. (e) Schematic of the gain medium and metal array. The SPs at the $\mathbf{K}$ and $\mathbf{K}'$ points compete for the same gain.

where $\hat{a}^{\dagger}_{\nu\mathbf{k}}$ and $\hat{a}_{\nu\mathbf{k}}$ are the SP creation and annihilation operators. Here the frequency $\omega_{\nu\mathbf{k}}$ is found from equation $\mathrm{Re}[s(\omega_{\nu\mathbf{k}})] = s_{\nu\mathbf{k}}$, where $s(\omega) = \epsilon_d/[\epsilon_d - \epsilon_m(\omega)]$ is Bergman's spectral parameter, ϵ_d and $\epsilon_m(\omega)$ are the permittivities of the host material and the metal, respectively. The corresponding electric field is given by [1]

$$\mathbf{E}(\mathbf{r}, t) = -\sum_{\mathbf{k}=\mathbf{K},\mathbf{K}'} A_{\nu\mathbf{k}} \nabla\varphi_{\nu\mathbf{k}}(\mathbf{r})(\hat{a}_{\nu\mathbf{k}} + \hat{a}^{\dagger}_{\nu\mathbf{k}}), \tag{7}$$

where $A_{\nu\mathbf{k}} = \sqrt{4\pi\hbar s_{\nu\mathbf{k}}/\epsilon_d s'_{\nu\mathbf{k}}}$, $s'_{\nu\mathbf{k}} = \mathrm{Re}[ds(\omega)/d\omega|_{\omega=\omega_{\nu\mathbf{k}}}]$.

The gain medium is assumed to be achiral consisting of chromophores with a linear transition dipole moment $\mathbf{d}^{(p)}$ where p is a chromophore's number; this dipole equally couples to both the $\mathbf{K}$ and $\mathbf{K}'$ SP modes. The gain medium is described quantum mechanically using density matrix $\rho^{(p)}$. Within the rotating wave approximation (RWA), the nondiagonal elements of the density matrix can be written as $(\rho^{(p)})_{12} = \bar{\rho}^{(p)} \exp(i\omega_{\nu\mathbf{K}} t)$, while the diagonal elements determine the population inversion, $n^{(p)} = \rho^{(p)}_{22} - \rho^{(p)}_{11}$. The interaction between the gain medium and the SP system is determined by Hamiltonian

$$H_{\mathrm{int}} = -\sum_{p} \mathbf{E}(\mathbf{r}^{(p)}, t)\mathbf{d}^{(p)}. \tag{8}$$

Following Ref. [3], we treat the SPs quasiclassically by replacing the creation and annihilation operators by the respective complex c-number amplitudes $a^{*}_{\nu\mathbf{K}}$, $a_{\nu\mathbf{K}}$, and $a^{*}_{\nu\mathbf{K}'}$, $a_{\nu\mathbf{K}'}$. The corresponding SP population numbers per the composite unit cell are $N_{\mathbf{K}} = |a_{\nu\mathbf{K}}|^2$ and $N_{\mathbf{K}'} = |a_{\nu\mathbf{K}'}|^2$.

The coupled system of equations [3], which describes both the SPs and the gain medium, has the form

$$\dot{a}_{\nu\mathbf{K}} = -\gamma_{\mathrm{SP}} a_{\nu\mathbf{K}} + iN_{\mathrm{g}} \sum_{p} \bar{\rho}^{(p)*} \tilde{\Omega}^{(p)*}_{\nu\mathbf{K}}, \tag{9}$$

$$\dot{a}_{\nu\mathbf{K}'} = -\gamma_{\mathrm{SP}} a_{\nu\mathbf{K}'} + iN_{\mathrm{g}} \sum_{p} \bar{\rho}^{(p)*} \tilde{\Omega}^{(p)*}_{\nu\mathbf{K}'}, \tag{10}$$

$$\dot{n}^{(p)} = -4\mathrm{Im}\left(\bar{\rho}^{(p)} \sum_{\mathbf{k}=\mathbf{K},\mathbf{K}'} \tilde{\Omega}^{(p)}_{\nu\mathbf{k}} a^{(p)}_{\nu\mathbf{k}}\right) + g(1 - n^{(p)}) - \gamma_2(1 + n^{(p)}), \tag{11}$$

$$\dot{\bar{\rho}}^{(p)} = -\Gamma_{12}\bar{\rho}^{(p)} + in^{(p)} \sum_{\mathbf{k}=\mathbf{K},\mathbf{K}'} \tilde{\Omega}^{(p)*}_{\nu\mathbf{k}} a^{(p)*}_{\nu\mathbf{k}}. \tag{12}$$

Here index p numbers nanoshells (all the chromophores in a given nanoshell have the same density matrix), N_g is the number of chromophores of the gain medium inside each shell, γ_{SP} is the SP relaxation rate, γ_2 is the nonradiative decay rate of level $|2\rangle$ of the chromophore, Γ_{12} is polarization relaxation rate for the $|2\rangle \to |1\rangle$ transition of the chromophores, g is the pumping rate per a chromophore, and $\tilde{\Omega}^{(p)}_{\nu\mathbf{k}} = (1/\hbar)A_{\nu\mathbf{k}}\nabla\varphi_{\nu\mathbf{k}}(\mathbf{r}^{(p)})\mathbf{d}^{(p)}$ is the Rabi frequency. In computations, we set $\epsilon_d = 2$, $d = 10$ debye, $N_{\mathrm{g}} = 514$, $\gamma_{\mathrm{SP}} = 4.1 \times 10^{13}\ \mathrm{s}^{-1}$, $\Gamma_{12} = 2.1 \times 10^{14}\ \mathrm{s}^{-1}$, and $\gamma_2 = 4 \times 10^{12}\ \mathrm{s}^{-1}$. We used dielectric data [36] for silver as the nanoshells' metal.

The Rabi frequencies, $\tilde{\Omega}^{(p)}_{\nu\mathbf{K}}$ and $\tilde{\Omega}^{(p)}_{\nu\mathbf{K}'}$, are periodic on the lattice with the periods that are determined by the crystal momenta $\mathbf{K}$ and $\mathbf{K}'$, respectively. Any solution of Eqs. (9)–(12), which contains both the $\mathbf{K}$ and $\mathbf{K}'$ components, will be periodic on a superlattice with an 18-nanoshell unit cell ("supercell"), as shown in Fig. 1. The summation over p in Eqs. (9) and (10) is extended over the corresponding eighteen points.

As we have already stated in the introductory part, the specific selection of the valley where the spasing occurs is due to random fluctuations in the initial SP number due to quantum fluctuations, which we emulate by the initial

conditions. For Eqs. (9)–(12), we set $n^{(p)}(t)|_{t=0} = -1$, which implies that initially all the chromophores of the gain medium are in the ground state. Similarly, we assume that initially there is no polarization, $\bar{\rho}(t)|_{t=0} = 0$. With respect to the initial SP amplitudes, $a_{\nu\mathbf{K}}$ and $a_{\nu\mathbf{K}'}$, we consider three cases: (i) the initial SP amplitude is small and located only at the $\mathbf{K}$ point where we set $a_{\nu\mathbf{K}} = 0.1$ and $a_{\nu\mathbf{K}'} = 0$; (ii) the same as the previous case but with the SP amplitude located at the $\mathbf{K}'$ point, $a_{\nu\mathbf{K}} = 0$ and $a_{\nu\mathbf{K}'} = 0.1$; (iii) the SPs are initially present at both the $\mathbf{K}$ and $\mathbf{K}'$ points but with different amplitudes, $a_{\nu\mathbf{K}} = 1$ and $a_{\nu\mathbf{K}'} = 0.2$.

We start with case (iii) where initially both the $\mathbf{K}$ and $\mathbf{K}'$ valleys are weakly populated, with a higher population at the $\mathbf{K}$ point, which emulates a random initial condition created by quantum fluctuations. The pumping begins at $t = 0$ with a rate of $g = 10^{13}$ s^{-1}. The dynamics of the SP populations in both the valleys as a function of time t after the beginning of the pumping is displayed in Fig. 4(a). As we see, after the initial period of decay and relaxation oscillations, the population of the dominant $\mathbf{K}$ valley starts growing exponentially and then levels off becoming stationary with the SP population $N_{\mathbf{K}} \approx 150$. At the same time, the minor SP population, $N_{\mathbf{K}'}$, decays exponentially for $t \gtrsim 200$ fs. This occurs due to a strong competition of the $\mathbf{K}$ and $\mathbf{K}'$ modes for the common gain. At the same time, the decay to zero, $N_{\mathbf{K}'} \to 0$, implies that there is no cross-mode talk, which is due to the topological protection: these two SP modes carry conserved topological charges $Q_T = \pm 1$. Due to the $\mathcal{T}$ symmetry, the valleys are symmetric: starting with the $\mathbf{K}'$ valley with a dominant SP population, the final population will only be in that valley. Thus the topological spaser is a topologically protected symmetric bistable device.

The kinetics of the topological spaser, i.e., the dependence of the stationary SP population numbers, $N_{\mathbf{K}}$ and $N_{\mathbf{K}'}$ for $t \to \infty$, as functions of the pumping rate g, is illustrated in Fig. 4(b) for case (i) when only the $\mathbf{K}$ valley has a nonzero initial population: $N_K = 0.01$ and $N_{\mathbf{K}'} = 0$. There is a pronounced threshold after which the SP population in the $\mathbf{K}$ valley grows linearly with the pumping rate. The population in the $\mathbf{K}'$ valley remains zero due to the topological protection. Similarly, in case (ii), the SP population will be amplified and remain only in the $\mathbf{K}'$ valley.

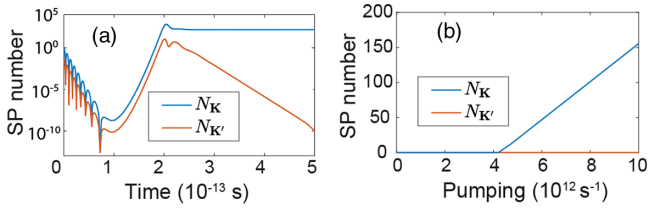

FIG. 4. Dynamics of SP population per unit supercell. (a) Temporal dynamics of the SP population. Initially the SPs in both the valleys are present, which is case (iii)—see the text. The pumping rate is $g = 10^{13}$ s^{-1}. (b) The stationary number of SPs in both valleys as a function of pumping rate.

The dynamics of the real-space distributions of the local fields in the topological spaser is shown in Figs. 5(a)–5(e) for the case of the $\mathbf{K}$-valley generation (see also the Supplemental Material [32] for the $\mathbf{K}'$ mode). The fields are normalized to one SP in the unit supercell. This distribution contains three dipolar fields localized on the A sublattice nanoshells, which rotate clockwise in the optical cycle. This field distribution is generally chiral and compliant with the E' representation of the D_{3h} group. At a given moment of time, this field distribution can also be described as a chiral lattice wave propagating in the clockwise direction along the unit cell boundary. The 2D E' representation also describes a mode with the opposite (counterclockwise) chirality, which can be obtained by an application of either $\mathcal{T}$ or σ_v' symmetry operations.

The present topologically charged E' spasing mode is indeed dark: obviously, it does not possess a net dipole moment. However, there is a nonzero chiral current propagating unidirectionally clockwise (for $Q_T = 1$) or counterclockwise (for $Q_T = -1$) within the A sublattice unit cell. Such currents for the neighboring cells cancel out each other. However, there will be an uncompensated chiral current at the edge of the 2D plasmonic lattice, which is illustrated in Fig. 5(e). The corresponding local fields resemble a field of a plasmon polariton propagating clockwise along the edge despite the absence of the edge states, similar to the edge plasmon polaritons in Ref. [33].

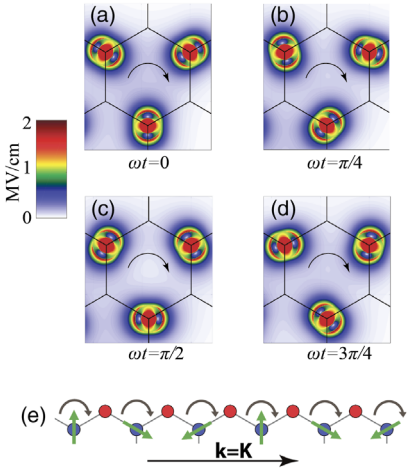

FIG. 5. Dynamics of $\mathbf{K}$-valley SP eigenmode. (a)–(d) The distributions of the local field modulus are plotted for the unit cell in the real space. The phases of the spaser oscillations are indicated. The color-coded scale of the local fields is given at the left-hand side for one SP quantum per the unit supercell. The local fields rotate in time in the direction of the black arrow, i.e., clockwise. (e) Edge fields for $\mathbf{K}$-valley mode. The instantaneous dipole vectors are indicated by the green arrows; the direction of the field rotation is depicted by the curved black arrows; crystal momentum $\mathbf{k}$ of the mode is shown by the straight black arrow. Each such a rotating dipole generates a current that is normal to this dipole.

There is the second E' mode of the same frequency, which is related to the above-discussed right-rotating one by the application of either $\mathcal{T}$ or σ_v' symmetry operations. That mode is generated in the K' valley; it is rotating counterclockwise within the unit cell and propagating counterclockwise along the edge. The choice of which one of these modes will be generated is random and is a spontaneous violation of the $\mathcal{T}$ and σ_v' symmetries. Figure 4 suggests a systematic way to break the $\mathcal{T}$ symmetry: initially preinject SPs with a desired chirality at the SP frequency, ω_{SP}. In contrast, a chiral (circularly polarized) pump will have no effect on the mode chirality because the gain medium is achiral.

In conclusion, we propose a topological spaser constituted by a honeycomb lattice of spherical metal nanoshells containing a gain medium. The two sublattices, A and B, are built from two different types of nanoshells. Such a spaser generates one of two chiral plasmonic modes characterized by topological charge $Q_T = \pm 1$ whose local fields rotate clockwise or counterclockwise, respectively. Which of these two modes is generated is determined by a spontaneous violation of symmetry as defined by the initial conditions. The chirality of the spasing mode is stable and topologically protected. The macroscopic fields of the spasing mode are localized along the edge of the lattice despite the absence of the edge states. These edge fields propagate clockwise (for $Q_T = 1$) or counterclockwise ($Q_T = -1$). Due to a very high lattice momentum $\mathbf{k} = \mathbf{K}$ or $\mathbf{k} = \mathbf{K}'$, they are dark in contrast to the original lasing spaser of Ref. [7]. Nevertheless, they can be outcoupled by using a corresponding coupler, e.g., grating. Application wise, such a topological spaser is a symmetric bistable that can be used for ultrafast optical storage and processing of information. Another class of perspective applications includes those in biomedical sensing and detection with an advantage of detecting the chirality that biological objects typically possess.

Major funding was provided by Grant No. DE-FG02-11ER46789 from the Materials Sciences and Engineering Division of the Office of the Basic Energy Sciences, Office of Science, U.S. Department of Energy. Numerical simulations have been performed using support by Grant No. DE-FG02-01ER15213 from the Chemical Sciences, Biosciences and Geosciences Division, Office of Basic Energy Sciences, Office of Science, US Department of Energy. The work of V. A. was supported by NSF EFRI NewLAW Grant No. EFMA-1741691. Support for J. W. came from a MURI Grant No. N00014-17-1-2588 from the Office of Naval Research (ONR).

*b91202047@gmail.com
†vapalkov@gsu.edu
‡mstockman@gsu.edu

[1] D. J. Bergman and M. I. Stockman, Surface Plasmon Amplification by Stimulated Emission of Radiation: Quantum Generation of Coherent Surface Plasmons in Nanosystems, Phys. Rev. Lett. **90**, 027402 (2003).
[2] M. I. Stockman and D. J. Bergman, Surface plasmon amplification by stimulated emission of radiation (spaser), US Patent 7,569,188 (2009).
[3] M. I. Stockman, The spaser as a nanoscale quantum generator and ultrafast amplifier, J. Optics **12**, 024004 (2010).
[4] K. Li, X. Li, M. I. Stockman, and D. J. Bergman, Surface plasmon amplification by stimulated emission in nanolenses, Phys. Rev. B **71**, 115409 (2005).
[5] D. Y. Fedyanin, Toward an electrically pumped spaser, Opt. Lett. **37**, 404 (2012).
[6] D. G. Baranov, A. P. Vinogradov, A. A. Lisyansky, Y. M. Strelniker, and D. J. Bergman, Magneto-optical spaser, Opt. Lett. **38**, 2002 (2013).
[7] N. I. Zheludev, S. L. Prosvirnin, N. Papasimakis, and V. A. Fedotov, Lasing spaser, Nat. Photonics **2**, 351 (2008).
[8] M. A. Noginov, G. Zhu, A. M. Belgrave, R. Bakker, V. M. Shalaev, E. E. Narimanov, S. Stout, E. Herz, T. Suteewong, and U. Wiesner, Demonstration of a spaser-based nanolaser, Nature (London) **460**, 1110 (2009).
[9] R. F. Oulton, V. J. Sorger, T. Zentgraf, R.-M. Ma, C. Gladden, L. Dai, G. Bartal, and X. Zhang, Plasmon lasers at deep subwavelength scale, Nature (London) **461**, 629 (2009).
[10] R.-M. Ma, R. F. Oulton, V. J. Sorger, G. Bartal, and X. Zhang, Room-temperature sub-diffraction-limited plasmon laser by total internal reflection, Nat. Mater. **10**, 110 (2011).
[11] R. A. Flynn, C. S. Kim, I. Vurgaftman, M. Kim, J. R. Meyer, A. J. Mäkinen, K. Bussmann, L. Cheng, F. S. Choa, and J. P. Long, A room-temperature semiconductor spaser operating near 1.5 micron, Opt. Express **19**, 8954 (2011).
[12] M. J. H. Marell, B. Smalbrugge, E. J. Geluk, P. J. van Veldhoven, B. Barcones, B. Koopmans, R. Nötzel, M. K. Smit, and M. T. Hill, Plasmonic distributed feedback lasers at telecommunications wavelengths, Opt. Express **19**, 15109 (2011).
[13] F. van Beijnum, P. J. van Veldhoven, E. J. Geluk, M. J. A. de Dood, G. W. tHooft, and M. P. van Exter, Surface Plasmon Lasing Observed in Metal Hole Arrays, Phys. Rev. Lett. **110**, 206802 (2013).
[14] Y.-J. Lu, C.-Y. Wang, J. Kim, H.-Y. Chen, M.-Y. Lu, Y.-C. Chen, W.-H. Chang, L.-J. Chen, M. I. Stockman, C.-K. Shih, and S. Gwo, All-color plasmonic nanolasers with ultralow thresholds: Autotuning mechanism for single-mode lasing, Nano Lett. **14**, 4381 (2014).
[15] Q. Zhang, G. Li, X. Liu, F. Qian, Y. Li, T. C. Sum, C. M. Lieber, and Q. Xiong, A room temperature low-threshold ultraviolet plasmonic nanolaser, Nat. Commun. **5**, 4953 (2014).
[16] B. T. Chou, Y. H. Chou, Y. M. Wu, Y. C. Chung, W. J. Hsueh, S. W. Lin, T. C. Lu, T. R. Lin, and S. D. Lin, Single-crystalline aluminum film for ultraviolet plasmonic nanolasers, Sci. Rep. **6**, 19887 (2016).
[17] C.-J. Lee, H. Yeh, F. Cheng, P.-H. Su, T.-H. Her, Y.-C. Chen, C.-Y. Wang, S. Gwo, S. R. Bank, C.-K. Shih, and W.-H. Chang, Low-threshold plasmonic lasers on a

single-crystalline epitaxial silver platform at telecom wavelength, ACS Photonics **4**, 1431 (2017).
[18] S. Sun, C. Zhang, K. Wang, S. Wang, S. Xiao, and Q. Song, Lead halide perovskite nanoribbon based uniform nanolaser array on plasmonic grating, ACS Photonics **4**, 649 (2017).
[19] R.-M. Ma, S. Ota, Y. Li, S. Yang, and X. Zhang, Explosives detection in a lasing plasmon nanocavity, Nat. Nanotechnol. **9**, 600 (2014).
[20] S. Wang, B. Li, X. Y. Wang, H. Z. Chen, Y. L. Wang, X. W. Zhang, L. Dai, and R. M. Ma, High-yield plasmonic nanolasers with superior stability for sensing in aqueous solution, ACS Photonics **4**, 1355 (2017).
[21] X. Y. Wang, Y. L. Wang, S. Wang, B. Li, X. W. Zhang, L. Dai, and R. M. Ma, Lasing enhanced surface plasmon resonance sensing, Nanophotonics **6**, 472 (2017).
[22] E. I. Galanzha, R. Weingold, D. A. Nedosekin, M. Sarimollaoglu, J. Nolan, W. Harrington, A. S. Kuchyanov, R. G. Parkhomenko, F. Watanabe, Z. Nima, A. S. Biris, A. I. Plekhanov, M. I. Stockman, and V. P. Zharov, Spaser as a biological probe, Nat. Commun. **8**, 15528 (2017).
[23] W. Zhou, M. Dridi, J. Y. Suh, C. H. Kim, D. T. Co, M. R. Wasielewski, G. C. Schatz, and T. W. Odom, Lasing action in strongly coupled plasmonic nanocavity arrays, Nat. Nanotechnol. **8**, 506 (2013).
[24] M. I. Stockman, Lasing spaser in two-dimensional plasmonic crystals, NPG Asia Mater. **5**, e71 (2013).
[25] M. V. Berry, Quantal phase factors accompanying adiabatic changes, Proc. R. Soc. Ser. A **392**, 45 (1984).
[26] D. Xiao, M.-C. Chang, and Q. Niu, Berry phase effects on electronic properties, Rev. Mod. Phys. **82**, 1959 (2010).
[27] R. Guo, M. Necada, T. K. Hakala, A. I. Vakevainen, and P. Torma, Lasing at k Points of a Honeycomb Plasmonic Lattice, Phys. Rev. Lett. **122**, 013901 (2019).
[28] Y. M. You, X. X. Zhang, T. C. Berkelbach, M. S. Hybertsen, D. R. Reichman, and T. F. Heinz, Observation of biexcitons in monolayer wse2, Nat. Phys. **11**, 477 (2015).
[29] K. S. Novoselov, A. Mishchenko, A. Carvalho, and A. H. C. Neto, 2d materials and van der Waals heterostructures, Science **353**, aac9439 (2016).
[30] D. N. Basov, M. M. Fogler, and F. J. G. de Abajo, Polaritons in van der Waals materials, Science **354**, aag1992 (2016).
[31] L. D. Landau and E. M. Lifshitz, *Quantum Mechanics: Non-Relativistic Theory* (Pergamon Press, Oxford and New York, 1965).
[32] See the Supplemental Material at http://link.aps.org/supplemental/10.1103/PhysRevLett.124.017701 for derivation of the tight-binding Schrodinger equation, calculations of the point-symmetry group characters for the mode obtained and identification of its representation, and additional graphics information.
[33] J. C. W. Song and M. S. Rudner, Chiral plasmons without magnetic field, Proc. Natl. Acad. Sci. U.S.A. **113**, 4658 (2016).
[34] D. J. Bergman and D. Stroud, Properties of macroscopically inhomogeneous media, in *Solid State Physics*, edited by H. Ehrenreich and D. Turnbull (Academic Press, Boston, 1992), Vol. 46, pp. 148–270.
[35] M. I. Stockman, S. V. Faleev, and D. J. Bergman, Localization Versus Delocalization of Surface Plasmons in Nanosystems: Can One State have Both Characteristics?, Phys. Rev. Lett. **87**, 167401 (2001).
[36] P. B. Johnson and R. W. Christy, Optical constants of noble metals, Phys. Rev. B **6**, 4370 (1972).